

EFFECT OF CAPILLARY PRESSURE ON SEISMIC VELOCITIES AND ATTENUATION

Khemraj Shukla,¹ José M. Carcione,^{2,6} Priyank Jaiswal,¹ Juan Santos,^{3,4,5} & Jing Ba^{6,*}

¹Boone Pickens School of Geology, 105 Noble Research Center, Oklahoma State University, Stillwater, OK, 74078.

²Istituto Nazionale di Oceanografia e di Geofisica Sperimentale (OGS), Borgo Grotta Gigante 42c, 34010 Sgonico, Trieste, Italy.

³CONICET, Instituto del Gas y del Petróleo, Facultad de Ingeniería, Universidad de Buenos Aires, Av. Las Heras 2214 Piso 3, C1127AAR Buenos Aires, Argentina.

⁴Department of Mathematics, Purdue University, 150 N. University Street, West Lafayette, Indiana, 47907-2067, USA.

⁵Universidad Nacional de La Plata, Argentina.

⁶School of Earth Science and Technology, Hohai University, Nanjing, 211100, China

*Address all correspondence to: Jing Ba, School of Earth Science and Technology, Hohai University, Nanjing, 211100, China, E-mail: 20160019@hhu.edu.cn

Original Manuscript Submitted: 08/15/2017; Final Draft Received: 11/26/2017

Biot's theory allows incorporation of permeability and viscosity in computing seismic amplitudes for a porous medium that is fully saturated with a single-phase fluid. In its original form, Biot's theory does not explicitly account for capillary effects, e.g., the surface tension between the wetting and non-wetting fluids. This paper uses a model to quantify capillary effects on velocity and attenuation. Studies that have attempted to extend Biot's poroelasticity to include capillary effects found changes in fast P-wave velocity of up to 5 % between the sonic and ultrasonic frequency ranges. Simulations of wave propagation at varying capillary pressure in a rock saturated with multi-phase fluid are also presented. The poroelastic equation for multi-phase fluid is solved by using spectral methods with Fourier grids as collocation points in space and the Runge-Kutta scheme for numerical integration. The numerical simulations show the presence of three compressional (P-) waves, one fast and two slow compressional waves corresponding to the wetting and non-wetting phases. The results show that the slow P-wave amplitude is significantly affected by capillary pressure variations.

KEY WORDS: Capillary pressure, Seismic velocity, Pseudo-spectral, Biot's model

1. INTRODUCTION

Wave propagation in porous media (poroelasticity) has been a subject of great interest for geophysicists and engineers alike (Allard and Atalla, 2009; Carcione, 2014). The foundation of poroelasticity was laid down through a series of seminal works in Biot (1956a,b, 1962). The premise of poroelasticity is that wave propagation sets both solid and fluid particles in relative motion, and, therefore the energy is propagated through the frame as well as through the pore fluid, with the competing driving forces of inertial and viscous nature depending on the frequency range. Three modes of energy propagation exist in the body, i.e., two compressional (P) (a fast and a slow) and one shear (S) (Biot, 1956a,b). In contrast, elastic modeling assumes that the propagation media is fully solid and the energy propagates only through P and S modes.

The slow P-wave, which is unique to the poroelastic model, is a diffusive mode of energy propagation that originates from the relative motion between solid and fluid particles. The polarization of the fast P-wave is described by in-phase motion between the solid and fluid particles and the polarization of the slow P-wave is described by the out of phase motion between solid and fluid particles. At frequencies < 100 Hz, the viscous forces generally dominate over the inertial forces attenuating the slow P-wave in the near-field (Carcione and Quiroga-Goode, 1995). On the other hand, at frequencies > 1 kHz, inertial forces are dominant over viscous forces and energy contained in the slow P-wave can be significant allowing it to be recorded in the far-field. The first clear documentation of the slow P-wave was at ultrasonic frequencies in a laboratory setting in water saturated sintered glass beads (18.5 % porosity) with velocity of 1040 m/sec (Plona, 1980). However, before Biot predicted it, Oura (1952) reported experimental values of the slow P-wave velocity in snow.

The limitation of Biot's theory in predicting wave attenuation for complex pores and multi-phase fluid has been alluded towards by several researchers (Mochizuki, 1982; Stoll and Bryan, 1970). In principle, a complex pore geometry and presence of two or more immiscible fluid phases results in complex relaxation for both fluid and solid phases. In Biot (1956a,b) the relaxation term is a visco-dynamic operator which in essence is the frequency-dependent permeability also known as the dynamic permeability term (Johnson et al., 1987). Santos et al. (1990a) and Santos et al. (1990b) extended Biot's theory to multi-phase fluid media by making this visco-dynamic term a capillary pressure (Dejam et al., 2015) dependent, where capillary forces exclusively imply surface tension due to the wetting and non-wetting fluid phases (see also Ravazzoli et al. (2003), Santos et al. (2013) and Santos et al. (2016)). Recently, Santos et al. (2017) have analyzed the dependence of the phase velocities of the slow P-waves (prevalent in poroelastic media saturated with single to multiphase fluids) on saturation of non-wetting phase (gas) and depth. In brief, the outcome of this study shows that the velocities of the slow wave in the ultrasonic frequency range (P2 and P3 modes) generally decrease as the saturation of non-wetting phase decreases, similar to the present study, wherein the velocity of the slow P-wave modes decreases as capillary pressure increases. In addition to this, those authors have also shown that the velocity of the slow P-wave modes increases as pore pressure increases, where pore pressure is alluded as function of depth.

Other wave propagation theories considering the capillary pressure were developed by Auriault et al. (1989), Lo et al. (2005), Lu et al. (2007), Tian et al. (2010) and Qi et al. (2014). Auriault et al. (1989) use a homogenization theory and a description of the capillary effects at the pore scale, obtaining a generalized Darcy law. Lo et al. (2005) derived a model for waves traveling in an elastic porous solid permeated by two immiscible fluids incorporating both inertial and viscous drags in an Eulerian frame of reference, applying their model to a Columbia fine sandy loam saturated by air-water and oil-water. Lu et al. (2007) obtained a dynamic model for wave propagation in a porous medium saturated with two immiscible fluids by incorporating three kinds of relaxation mechanisms. These are based on a) A drag force model accounting for attenuation due to global fluid flow, b) A capillary-pressure based mechanism responsible for relaxation of the interface between the wetting and non-wetting fluid phases, and c) A porosity-based relaxation mechanism accounting for local fluid flow. A direct comparison between the present study and capillary-based relaxation model of Lu et al. (2007) differs in the method used to compute the capillary pressure. In the limiting case of $p_{ca} = 0$, the non-wetting phase saturation S_n in Lu et al. (2007) model is dependent on the irreducible saturation of the wetting phase (S_{rw}), whereas in our model the non-wetting phase saturation S_n is a function of the irreducible saturation of the wetting S_{rw} and non-wetting phase S_{rn} . Thus the capillary pressure model used in the present study defines the concept of relative permeability between the multiphase fluid with saturation more accurately. Lu et al. (2007) have shown the variation of velocity and attenuation with respect to the capillary pressure dependent modulus (see their Figs. 2 and 3) unlike in the present study, where the direct dependence on capillary pressure is shown. In general, the attenuation of the P wave increases for certain values of the capillary parameter (see their Fig. 5b). The effect of varying capillary pressures on the numerical solution is not shown in Lu et al. (2007). Tian et al. (2010) use a theory similar to that of the present work and find that the capillary pressure greatly affects the displacement of the non-wetting phase (oil or gas in a water saturated background). Qi et al. (2014) studied the effect of capillary pressure on the acoustic signature in the framework of the mesoscopic-loss theory. In this study the effect of capillarity was induced through the incorporation of a membrane stiffness in a random medium of patchy saturation. The capillary action leads to an additional stiffening and thereby to higher phase velocities. It also implies a pressure discontinuity at patch interfaces so that wave-induced pressure diffusion process is weakened and attenuation

is reduced.

In another experimental modeling study by Liu et al. (2016), the P-wave velocity for variable fluid patch sizes is studied, with the patch size being a function of the fluid saturation. In this study, the effect of capillarity is linked to the injection rate, which changes during imbibition due to the redistribution of the viscous and capillary pressure in rock samples. The very idea of this study is based on the redistribution of capillary effects, which in turn changes the stiffness of the fluid-rock system resulting into changes in the rock velocity. According to this concept, Liu et al. (2016) has shown that the overall effect of increasing capillarity causes an increase in static velocity of the P wave (measured experimentally) (see their Figure 6). Unlike our study, they have not mentioned anything about the effects of capillarity on slow P waves and also lacks the representation of the effect of capillarity on numerical simulation of wave propagation.

In another study of wave propagation in rocks saturated with two immiscible fluid, Papageorgiou and Chapman (2017) simulated the effect of squirt flow on the P-wave velocity of a rock saturated with water and CO₂. In this study, the authors considered a static dimensionless capillary function bounded above and below by 1 and the ratio of bulk modulus of gas and water, respectively. The modeling approach adopted in the study only models the fast P-wave and lacks the discussions about the slow P-wave modes. The results obtained in this study show that the velocity of the P wave at high frequencies, in general, increases with capillary pressure (see their Figure 4 and 5). In another result (see their Figure 4), the velocity of the P wave with respect to the wetting phase saturation has a similar trend as in Figure 1 of the present study. This study also lacks the wave field characteristics with respect to varying capillary pressure.

Extending Biot's theory into the capillary domain led to two key observations. First, a step change in fast P-wave velocity by up to 5 % occurs near the characteristic frequency of the medium (Carcione et al., 2004). Second, the relative motion between the non-wetting fluid phase and the solid grain gives rise to a second slow P-wave phase (Carcione et al., 2004; Santos et al., 2004). The first finding is of particularly relevant to quantitative interpretation of ultrasonic data, more so when velocity measurements at ultrasonic ranges on undrained core plugs are to be reconciled with the surface seismic velocities. The second finding is relevant in understanding the energy loss mechanism. Although peer studies have laid theoretical and numerical formulations for energy partitioning in presence of more than one fluid phase, the system has not been yet analyzed for varying capillary pressure. Here we analyze the body-wave velocities and their attenuation as a function of capillary pressure. We also present numerical solution for a two-phase fluid system (gas and water) with varying capillary pressure. Carcione et al. (2004) and Santos et al. (2004) have solved the equations developed by Santos et al. (1990b) using different numerical approaches. Here, we use the first method.

2. THEORY

Next, we present a summary of wave propagation in partially saturated porous medium developed by Santos et al. (1990b), Carcione et al. (2004), Ravazzoli et al. (2003) and Santos et al. (2013) guiding the reader to original references for detail.

2.1 Equations of momentum conservation

Let a porous rock saturated by two immiscible fluids denoted with the superscripts s , w and n corresponding to the solid, wetting and non-wetting phases, respectively. Let \mathbf{v}_s , $\bar{\mathbf{v}}^n$ and $\bar{\mathbf{v}}^w$ be particle velocity vectors for solid grain, wetting fluid and non-wetting fluid, respectively and let $\boldsymbol{\tau}$, $\boldsymbol{\tau}_n$ and $\boldsymbol{\tau}_w$ be the total stress tensor for solid, non-wetting phase and wetting phase respectively. Relative particle velocities for non-wetting and wetting phases are defined as: $\mathbf{v}^n = \phi(\bar{\mathbf{v}}^n - \mathbf{v}_s)$ and $\mathbf{v}^w = \phi(\bar{\mathbf{v}}^w - \mathbf{v}_s)$ respectively. The equations of momentum conservation for the solid,

wetting and non-wetting phases are

$$\nabla \cdot \boldsymbol{\tau} = \rho \dot{\mathbf{v}}_s + \rho_n S_n \dot{\mathbf{v}}^n + \rho_w S_w \dot{\mathbf{v}}^w, \quad (1)$$

$$\nabla \tau_n = \rho_n S_n \dot{\mathbf{v}}^s + g_1 \dot{\mathbf{v}}^n + g_3 \dot{\mathbf{v}}^w + S_n^2 \left(\frac{\eta_n}{\kappa_n} \right) \mathbf{v}^n, \quad (2)$$

$$\nabla \tau_w = \rho_w S_w \dot{\mathbf{v}}^s + g_3 \dot{\mathbf{v}}^n + g_2 \dot{\mathbf{v}}^w + S_w^2 \left(\frac{\eta_w}{\kappa_w} \right) \mathbf{v}^w, \quad (3)$$

where S , η , ρ , ϕ and κ are saturation ($S_n + S_w = 1$), viscosity, density, porosity and permeability, respectively. A dot above a variable represents the time derivative. The relative permeability of the non-wetting and wetting phases will be denoted by κ_n and κ_w . Santos et al. (1990b) define bulk density (ρ) and mass couple coefficients (g_1 : solid and non-wetting; g_2 : solid and wetting; and g_3 : non-wetting and wetting) as

$$\begin{aligned} \rho &= (1 - \phi)\rho_s + \phi(S_n\rho_n + S_w\rho_w), & g_1 &= \frac{S_n\rho_n F_s}{\phi}, \\ g_2 &= \frac{S_w\rho_w F_s}{\phi}, & g_3 &= 0.1\sqrt{g_1 g_2}, \end{aligned}$$

where F_s is a structural factor as in Berryman (1980). The capillary pressure $p_{ca} > 0$ (Santos et al., 1990b) is defined as

$$p_{ca} = A \left[(S_n + S_w - 1)^{-2} - \left(\frac{S_{rn}}{S_n} \right) (1 - S_{rn} - S_{rw})^{-2} \right], \quad (4)$$

where, S_{rn} and S_{rw} are residual saturations of the wetting and non-wetting phases. A is constant, constraining $p_{ca} > 0$. The permeabilities κ_n and κ_w are given as

$$\kappa_n = \kappa \left(1 - \frac{1 - S_n}{1 - S_{rn}} \right)^2, \quad \kappa_w = \kappa \left(\frac{1 - S_n - S_{rw}}{1 - S_{rw}} \right)^2,$$

where κ is absolute permeability.

2.2 Stress-strain relations

The 2D stress-strain relationship for the multi-phase system in the (x,y) -plane can be expressed as

$$\mathbf{S} = \mathbf{C} \cdot \mathbf{e}, \quad (5)$$

where $S = [\tau_{xx}, \tau_{yy}, \tau_{xy}, \tau_n, \tau_w]^T$, $\mathbf{e} = [\epsilon_{xx}, \epsilon_{yy}, \epsilon_{xy}, \zeta_n, \zeta_w]^T$ and

$$\mathbf{C} = \begin{pmatrix} K_c + N & K_c - N & 0 & -B_1 & B_2 \\ K_c - N & K_c + N & 0 & -B_1 & B_2 \\ 0 & 0 & 0 & 2N & 0 \\ B_1 & B_1 & 0 & -M_1 & -M_3 \\ B_2 & B_2 & 0 & -M_3 & -M_2 \end{pmatrix},$$

where ϵ 's are strain for solid phase and $\zeta_{n,w}$ are variations of fluid content defined as $\dot{\zeta}_{n,w} = -\nabla \cdot \mathbf{v}^{n(w)}$. In the stiffness matrix \mathbf{C} , K_c and N are undrained bulk and dry-rock shear moduli, respectively. Coefficients B_1 , B_2 , M_1 , M_2 and M_3 depend on rock and fluid type (Santos et al., 2013). To derive the dispersion relation, the stress induced in the non-wetting phase can be rewritten using first principles (Santos et al., 1990b)

$$\tau_n = -(S_n + \beta + \chi)p_n + (\beta + \chi)p_w, \quad (6)$$

where p_n and p_w are infinitesimal changes in the wetting and non-wetting fluid pressures from the absolute fluid pressure \bar{p}_n and \bar{p}_w . β and χ are parameters describing the capillary pressure and defined as $\beta = \frac{p_{ca}}{p'_{ca}}$, $\chi = \frac{\bar{p}_w}{p'_{ca}} \cdot p'_{ca}$

represent the change in capillary pressure with respect to the saturation of the non-wetting phase. Equations (2) and (6) imply that changes in stress in the non-wetting phase causes changes in the particle velocities (for both solid and relative fluid velocity). Equation (6) also implies that the stress in the non-wetting fluid phase is linearly dependent on p_{ca} , which is what in turn creates the dependence of seismic velocities on capillary pressure.

2.3 Particle velocity-stress relationship

The particle velocity-stress formulation defines the coupled system of partial differential equations which describes the wave propagation in a porous rock saturated with multi-phase fluids. Equation (1-3), can be rewritten as

$$v_i^s = \rho(\tau_{ix,x} + \tau_{iy,y}) + \rho_n S_n \left[\tau_{n,i} - S_n^2 \left(\frac{\eta_n}{\kappa_n} \right) v_i^n \right] + \rho_w S_w \left[\tau_{w,i} - S_w^2 \left(\frac{\eta_w}{\kappa_w} \right) v_i^w \right], \quad (7)$$

$$v_i^n = \rho_n S_n (\tau_{ix,x} + \tau_{iy,y}) + g_1 \left[\tau_{n,i} - S_n^2 \left(\frac{\eta_n}{\kappa_n} \right) v_i^n \right] + g_3 \left[\tau_{w,i} - S_w^2 \left(\frac{\eta_w}{\kappa_w} \right) v_i^w \right], \quad (8)$$

$$v_i^w = \rho_w S_w (\tau_{ix,x} + \tau_{iy,y}) + g_3 \left[\tau_{n,i} - S_n^2 \left(\frac{\eta_n}{\kappa_n} \right) v_i^n \right] + g_2 \left[\tau_{w,i} - S_w^2 \left(\frac{\eta_w}{\kappa_w} \right) v_i^w \right]. \quad (9)$$

Equations corresponding to stress components are obtained by differentiating (5) with respect to time and can be expressed as

$$\dot{\tau}_{xx} = K_c(\nabla \cdot \mathbf{v}^s) + N(v_{x,x} - v_{y,y}) + B_1(\nabla \cdot \mathbf{v}^n) + B_2(\nabla \cdot \mathbf{v}^w), \quad (10)$$

$$\dot{\tau}_{yy} = K_c(\nabla \cdot \mathbf{v}^s) - N(v_{x,x} - v_{y,y}) + B_1(\nabla \cdot \mathbf{v}^n) + B_2(\nabla \cdot \mathbf{v}^w), \quad (11)$$

$$\dot{\tau}_{xy} = N(v_{x,y} + v_{y,x}), \quad (12)$$

$$\dot{\tau}_n = B_1(\nabla \cdot \mathbf{v}^s) - M_1(\nabla \cdot \mathbf{v}^n) - M_3(\nabla \cdot \mathbf{v}^w), \quad (13)$$

$$\dot{\tau}_w = B_2(\nabla \cdot \mathbf{v}^s) - M_3(\nabla \cdot \mathbf{v}^n) - M_2(\nabla \cdot \mathbf{v}^w). \quad (14)$$

3. VELOCITY AND ATTENUATION

A succinct form of the first-order velocity-stress relation, describing the wave equation for partially saturated porous medium can be recovered by combining equations (7-9) and (10-14) and expressed as

$$\frac{d\mathbf{w}}{dt} = \mathbf{M}\mathbf{w} + \mathbf{f}, \quad (15)$$

where \mathbf{w} is the wavefield vector $\mathbf{w} = [v_x^s, v_x^n, v_x^w, v_y^s, v_y^n, v_y^w, \tau_{xx}, \tau_{yy}, \tau_{xy}, \tau_n, \tau_w]$ and \mathbf{f} is the forcing function, which is the product of the delta function and the Ricker wavelet in space and time domain, respectively, \mathbf{M} is the propagator matrix, containing the material coefficients and spatial derivatives:

$$\mathbf{M} = \begin{pmatrix} 0 & -\rho_n S_n^3 \left(\frac{\eta_n}{\kappa_n} \right) & -\rho_w S_w^3 \left(\frac{\eta_w}{\kappa_w} \right) & 0 & 0 & 0 & \rho \frac{\partial}{\partial x} & 0 & \rho \frac{\partial}{\partial y} & \rho_n S_n \frac{\partial}{\partial x} & \rho_w S_w \frac{\partial}{\partial x} \\ 0 & -g_1 S_n^2 \left(\frac{\eta_n}{\kappa_n} \right) & -g_3 S_w^2 \left(\frac{\eta_w}{\kappa_w} \right) & 0 & 0 & 0 & \rho_n S_n \frac{\partial}{\partial x} & 0 & \rho_n S_n \frac{\partial}{\partial y} & g_1 \frac{\partial}{\partial x} & g_3 \frac{\partial}{\partial x} \\ 0 & -S_n^2 \left(\frac{\eta_n}{\kappa_n} \right) & -S_w^2 \left(\frac{\eta_w}{\kappa_w} \right) & 0 & 0 & 0 & \rho_w S_w \frac{\partial}{\partial x} & 0 & \rho_w S_w \frac{\partial}{\partial y} & g_3 \frac{\partial}{\partial x} & g_2 \frac{\partial}{\partial x} \\ 0 & 0 & 0 & 0 & -\rho_n S_n^3 \left(\frac{\eta_n}{\kappa_n} \right) & -\rho_w S_w^3 \left(\frac{\eta_w}{\kappa_w} \right) & 0 & \rho \frac{\partial}{\partial y} & \rho \frac{\partial}{\partial x} & \rho_n S_n \frac{\partial}{\partial y} & \rho_w S_w \frac{\partial}{\partial y} \\ 0 & 0 & 0 & 0 & -g_1 S_n^2 \left(\frac{\eta_n}{\kappa_n} \right) & -g_3 S_w^2 \left(\frac{\eta_w}{\kappa_w} \right) & 0 & \rho_n S_n \frac{\partial}{\partial y} & \rho_n S_n \frac{\partial}{\partial x} & g_1 \frac{\partial}{\partial y} & g_3 \frac{\partial}{\partial y} \\ 0 & 0 & 0 & 0 & -g_3 S_n^2 \left(\frac{\eta_n}{\kappa_n} \right) & -g_2 S_w^2 \left(\frac{\eta_w}{\kappa_w} \right) & 0 & \rho_w S_w \frac{\partial}{\partial y} & \rho_w S_w \frac{\partial}{\partial x} & g_3 \frac{\partial}{\partial y} & g_2 \frac{\partial}{\partial y} \\ (K_c + N) \frac{\partial}{\partial x} & B_1 \frac{\partial}{\partial x} & B_2 \frac{\partial}{\partial x} & (K_c - N) \frac{\partial}{\partial y} & B_1 \frac{\partial}{\partial y} & B_2 \frac{\partial}{\partial y} & 0 & 0 & 0 & 0 & 0 \\ (K_c - N) \frac{\partial}{\partial x} & B_1 \frac{\partial}{\partial x} & B_2 \frac{\partial}{\partial x} & (K_c + N) \frac{\partial}{\partial y} & B_1 \frac{\partial}{\partial y} & B_2 \frac{\partial}{\partial y} & 0 & 0 & 0 & 0 & 0 \\ N \frac{\partial}{\partial y} & 0 & 0 & N \frac{\partial}{\partial x} & 0 & 0 & 0 & 0 & 0 & 0 & 0 \\ B_1 \frac{\partial}{\partial x} & -M_1 \frac{\partial}{\partial x} & -M_3 \frac{\partial}{\partial x} & B_1 \frac{\partial}{\partial y} & -M_1 \frac{\partial}{\partial y} & -M_3 \frac{\partial}{\partial y} & 0 & 0 & 0 & 0 & 0 \\ B_2 \frac{\partial}{\partial x} & -M_3 \frac{\partial}{\partial x} & -M_2 \frac{\partial}{\partial x} & B_2 \frac{\partial}{\partial y} & -M_3 \frac{\partial}{\partial y} & -M_2 \frac{\partial}{\partial y} & 0 & 0 & 0 & 0 & 0 \end{pmatrix}. \quad (16)$$

To analyze the dependence of the phase velocities of each mode present in equation (15) requires a dispersion relations for a plane wave. A compressional plane wave propagating in a medium with an attenuation factor α , a complex wavevector $\mathbf{k} = \mathbf{k} - i\alpha$ and an angular frequency of ω , can be expressed as

$$\mathbf{q} = \mathbf{q}_0 \exp(\mathbf{k} \cdot \mathbf{x} - \omega t), \quad (17)$$

where $\mathbf{q} = [\epsilon, \zeta_n, \zeta_w]^T$ and \mathbf{q}_0 is the polarization vector of the compressional modes present in the system. The dispersion relation for a plane wave (Equation (17)) governed by Equation (15) is expressed as (Carcione et al., 2004)

$$\mathbf{\Gamma} \mathbf{q}_0 = v_c^2 (\mathbf{D} - i\mathbf{L}) \mathbf{q}_0, \quad (18)$$

where $\mathbf{\Gamma}$, \mathbf{D} and \mathbf{L} are stiffness, density and friction matrices.

The three eigenvalues (v_c)s of Equation (18) correspond to three P-wave phases with velocities (v_p)s and attenuation (α)s are

$$v_p = \left[\text{Re} \left(\frac{1}{v_c} \right) \right]^{-1}, \quad \alpha = -\omega \left[\text{Im} \left(\frac{1}{v_c} \right) \right]. \quad (19)$$

Following Santos et al. (1990b), the phase velocity of the shear wave is governed by the rotational part of Equations (1-3). Operating Equation (1-3) with the curl ($\nabla \times$) operator and using the vector identity $\mathbf{a} \cdot (\mathbf{a} \times \mathbf{b}) = 0$, we get

$$\rho(\nabla \times \dot{\mathbf{v}}_s) + \rho_n S_n (\nabla \times \dot{\mathbf{v}}^n) + \rho_w S_w (\nabla \times \dot{\mathbf{v}}^w) = N(\epsilon_{xxx,x} + \epsilon_{yy,y}), \quad (20)$$

$$\rho_n S_n (\nabla \times \dot{\mathbf{v}}^s) + g_1 (\nabla \times \dot{\mathbf{v}}^n) + g_3 (\nabla \times \dot{\mathbf{v}}^w) + S_n^2 \left(\frac{\eta_n}{\kappa_n} \right) (\nabla \times \mathbf{v}^n) = 0, \quad (21)$$

$$\rho_w S_w (\nabla \times \dot{\mathbf{v}}^s) + g_3 (\nabla \times \dot{\mathbf{v}}^n) + g_2 (\nabla \times \dot{\mathbf{v}}^w) + S_w^2 \left(\frac{\eta_w}{\kappa_w} \right) (\nabla \times \mathbf{v}^w) = 0. \quad (22)$$

Analytical expressions of $\bar{\mathbf{V}} (\nabla \times (\mathbf{v}^s, \mathbf{v}^n, \mathbf{v}^w))$ can be expressed as,

$$\bar{\mathbf{V}} = \bar{\mathbf{V}}_0 e^{i(\mathbf{k} \cdot \mathbf{x} - \omega t)}. \quad (23)$$

where $\bar{\mathbf{V}}_0$ is the polarization vector of the shear modes present in the system. Substituting Equation (23) in Equations (20-22), we obtain the phase velocity of shear wave, which is

$$v_c = \sqrt{N} \left[\rho - \frac{C_1 + C_2}{g_1^* g_2^* - g_3^2} \right]^{-1/2}, \quad (24)$$

where $C_1 = \rho_n S_n (g_3^* \rho_n S_n - g_3 \rho_w S_w)$, $C_2 = \rho_w S_w (g_1^* \rho_w S_w - g_3 \rho_n S_n)$, $g_1^* = g_1 - \frac{ib_n}{\omega}$ and $g_3^* = g_3 - \frac{ib_w}{\omega}$.

4. NUMERICAL-SIMULATION METHOD

The next step is to adopt a stable numerical scheme to solve Equation (15), which requires a detailed analysis of the eigenvalues of the propagator matrix \mathbf{M} . As a clarification the largest and the smallest eigenvalues represent velocities of the fast and slow P- modes respectively. Eigenvalues of \mathbf{M} are complex conjugates pairs. For non-viscous pore-fluids the eigenvalues are purely imaginary but for a viscous fluid they also have a real part which is negative and which represents attenuation. For the Nivelsteiner sandstone (Table 1), the real part of the largest and smallest eigenvalues are -145467 s^{-1} and -1274 s^{-1} , respectively. A large difference in magnitude of the eigenvalues makes the system stiff (Jain, 1979) and requires the modeling scheme to have very small time steps for being numerically stable and accurate at the same time.

Santos et al. (2004) and Carcione et al. (2004) solved Equation (15) numerically by adopting different approaches. Santos et al. (2004) computed the numerical solution in the frequency domain, similar to the form of a Helmholtz equation. At each time step the numerical solution is obtained by solving the system of Helmholtz-like equations across the entire frequency range without any constraint on the choice of the time step (CFL condition). Thus, the problem of stiffness is taken care implicitly at the cost of an added computational complexity. On the other hand, Carcione et al. (2004) solved Equation (15) in the time domain and circumvented the effect of stiffness by adopting the approach of Carcione and Seriani (2001). In this paper, we have followed Carcione et al. (2004) to solve Equation

(15) numerically. This approach firstly separates Equation (15) into stiff and non-stiff parts to circumvent the stiffness of the system, secondly it solves them separately and finally merges the solutions obtained from the previous two steps. The spatial derivatives of \mathbf{M} are computed by using the Fourier method (Carcione, 2014) and the equation is integrated in time with the fourth-order Runge-Kutta method. A brief review of the numerical methods is presented in the following.

The formal solution of Equation (15) is given by (Carcione et al., 2002)

$$\mathbf{w}(t) = \exp(t\mathbf{M})\mathbf{w}_0 + \int_0^t \exp(\tau\mathbf{M})f(t - \tau)d\tau, \quad (25)$$

where \mathbf{w}_0 is the initial condition and $\exp(t\mathbf{M})$ is known as the evolution operator. The splitting algorithm (Carcione and Seriani, 2001) partitions \mathbf{M} as $\mathbf{M} = \mathbf{M}_r + \mathbf{M}_s$ with \mathbf{M}_r and \mathbf{M}_s representing the stiff and non-stiff part of \mathbf{M} respectively and expressed as

$$\mathbf{M}_r = \left(\begin{array}{c|c} 0_{6 \times 5} & \mathbf{M}_{r1} \\ \hline \mathbf{M}_{r2} & 0_{5 \times 5} \end{array} \right), \quad (26)$$

where

$$\mathbf{M}_{r1} = \begin{pmatrix} \rho \frac{\partial}{\partial x} & 0 & \rho \frac{\partial}{\partial y} & \rho_n S_n \frac{\partial}{\partial x} & \rho_w S_w \frac{\partial}{\partial x} \\ \rho_n S_n \frac{\partial}{\partial x} & 0 & \rho_n S_n \frac{\partial}{\partial y} & g_1 \frac{\partial}{\partial x} & g_3 \frac{\partial}{\partial x} \\ \rho_w S_w \frac{\partial}{\partial x} & 0 & \rho_w S_w \frac{\partial}{\partial y} & g_3 \frac{\partial}{\partial x} & g_2 \frac{\partial}{\partial x} \\ 0 & \rho \frac{\partial}{\partial y} & \rho \frac{\partial}{\partial x} & \rho_n S_n \frac{\partial}{\partial y} & \rho_w S_w \frac{\partial}{\partial y} \\ 0 & \rho_n S_n \frac{\partial}{\partial y} & \rho_n S_n \frac{\partial}{\partial x} & g_1 \frac{\partial}{\partial y} & g_3 \frac{\partial}{\partial y} \\ 0 & \rho_w S_w \frac{\partial}{\partial y} & \rho_w S_w \frac{\partial}{\partial x} & g_3 \frac{\partial}{\partial y} & g_2 \frac{\partial}{\partial y} \end{pmatrix}, \quad (27)$$

$$\mathbf{M}_{r2} = \begin{pmatrix} (K_c + N) \frac{\partial}{\partial x} & B_1 \frac{\partial}{\partial x} & B_2 \frac{\partial}{\partial x} & (K_c - N) \frac{\partial}{\partial y} & B_1 \frac{\partial}{\partial y} & B_2 \frac{\partial}{\partial y} \\ (K_c - N) \frac{\partial}{\partial x} & B_1 \frac{\partial}{\partial x} & B_2 \frac{\partial}{\partial x} & (K_c + N) \frac{\partial}{\partial y} & B_1 \frac{\partial}{\partial y} & B_2 \frac{\partial}{\partial y} \\ N \frac{\partial}{\partial y} & 0 & 0 & N \frac{\partial}{\partial x} & 0 & 0 \\ B_1 \frac{\partial}{\partial x} & -M_1 \frac{\partial}{\partial x} & -M_3 \frac{\partial}{\partial x} & B_1 \frac{\partial}{\partial y} & -M_1 \frac{\partial}{\partial y} & -M_3 \frac{\partial}{\partial y} \\ B_2 \frac{\partial}{\partial x} & -M_3 \frac{\partial}{\partial x} & -M_2 \frac{\partial}{\partial x} & B_2 \frac{\partial}{\partial y} & -M_3 \frac{\partial}{\partial y} & -M_2 \frac{\partial}{\partial y} \end{pmatrix}. \quad (28)$$

Matrix \mathbf{M}_s can be expressed as

$$\mathbf{M}_s = \left(\begin{array}{c|c} \mathbf{R}_{6 \times 6} & 0_{6 \times 5} \\ \hline 0_{5 \times 6} & 0_{5 \times 5} \end{array} \right), \quad (29)$$

where

$$\mathbf{R} = \left(\begin{array}{c|c} \mathbf{S}_{3 \times 3} & 0_{3 \times 3} \\ \hline 0_{3 \times 3} & \mathbf{S}_{3 \times 3} \end{array} \right), \quad (30)$$

where

$$\mathbf{S} = \begin{pmatrix} 0 & -\rho_n S_n^3 \left(\frac{\eta_n}{\kappa_n} \right) & -\rho_w S_w^3 \left(\frac{\eta_w}{\kappa_w} \right) \\ 0 & -g_1 S_n^2 \left(\frac{\eta_n}{\kappa_n} \right) & -g_3 S_w^2 \left(\frac{\eta_w}{\kappa_w} \right) \\ 0 & -S_n^2 \left(\frac{\eta_n}{\kappa_n} \right) & -S_w^2 \left(\frac{\eta_w}{\kappa_w} \right) \end{pmatrix}. \quad (31)$$

The discretized evolution operator (Equation (25)) at time step dt can be expressed as

$$\exp(\mathbf{M}dt) = \exp\left(\frac{1}{2}\mathbf{M}_s\right) \exp\left(\frac{1}{2}\mathbf{M}_r\right) \exp\left(\frac{1}{2}\mathbf{M}_s\right). \quad (32)$$

Equation (32) allows to solve the stiff part of the system separately and we can write the differential equation for velocity vector $\mathbf{v} = [v_x^s, v_x^n, v_x^w, v_y^s, v_y^n, v_y^w]^T$ as,

$$\dot{\mathbf{v}} = \mathbf{R}\mathbf{v}. \quad (33)$$

The solution of Equation (33), denoted as \mathbf{w}^* , is treated as an intermediate corrector term and can be computed analytically. The evaluation of the non-stiff term is ($\exp(\mathbf{M}_r t)$) is performed with the Runge-Kutta scheme and the Fourier method. Thus, the numerical scheme used to solve the system (Equation (15)) is

$$\mathbf{w}^{n+1} = \mathbf{w}^* + \frac{1}{6}(dt)(2\Delta_1 + 2\Delta_2 + 2\Delta_3 + 2\Delta_4), \quad (34)$$

where

$$\begin{aligned} \Delta_1 &= \mathbf{M}_r \mathbf{w}^* + \mathbf{f}^n, \quad \Delta_2 = \mathbf{M}_r (\mathbf{w}^* + \frac{1}{2}(dt)\Delta_1) + \mathbf{f}^{n+1/2}, \\ \Delta_3 &= \mathbf{M}_r (\mathbf{w}^* + \frac{1}{2}(dt)\Delta_2) + \mathbf{f}^{n+1/2}, \quad \Delta_4 = \mathbf{M}_r (\mathbf{w}^* + dt\Delta_3) + \mathbf{f}^{n+1}. \end{aligned}$$

The numerical scheme expressed in Equation (34) is “infinitely” accurate in space and achieves second order accuracy in time. We also claim that the numerical scheme (Equation (34)) is bounded by accuracy than stability, as the system under the study is stiff. To prove the above claim, a convergence study is performed for a plane wave of which analytical solution is computed using Equation (15). Stress and velocity vectors of a plane wave with real wave vector \mathbf{k} (no attenuation) and angular frequency ω can be expressed as

$$\mathbf{T} = \mathbf{T}_0 e^{i(\mathbf{k}\cdot\mathbf{x} - \omega t)}, \quad (35)$$

$$\mathbf{V} = \mathbf{V}_0 e^{i(\mathbf{k}\cdot\mathbf{x} - \omega t)}, \quad (36)$$

where $\mathbf{T} = [\tau_{xx}, \tau_{yy}, \tau_{xy}, \tau_n, \tau_w]^T$ and $\mathbf{V} = [v_x^s, v_x^n, v_x^w, v_y^s, v_y^n, v_y^w]^T$. \mathbf{T}_0 and \mathbf{V}_0 are polarization vectors.

5. RESULTS

We illustrate our results using the properties of the Nivelsteiner Sandstone (Kelder and Smeulders, 1997) (Table 1), which is a Miocene age quartz dominated formation containing < 5% clay. We use 3 kPa as the value of A in Equation (4) after Santos et al. (2013). In the plots hereon P1 indicates the fast P wave, P2 and P3 the slow waves and S is the shear wave. The characteristic frequency for the Nivelsteiner sandstone is 10 kHz, when fluid flow in the pores changes from laminar to turbulent. For our purpose we change the capillary pressure by changing the water saturation; $S_w = 90\%$ corresponds to a p_{ca} of 3.22 kPa and $S_w = 10\%$ corresponds to a p_{ca} of 1.22 MPa.

We perform the basic model validation by predicting the P1 wave with respect to an increasing gas saturation (S_{nw} or S_g ; Figure 1). As seen in Figure 1, v_{P1} drops rapidly when S_g increases initially. As S_g increases further, v_{P1} slightly increases. This concurs with prevalent understanding about the behavior of gas-brine mixture in porous rocks

(e.g. Domenico (1976, 1977), Gomez et al. (2010)). Our model successfully explains the poromechanical behavior of a gas-brine mixture. For computing Figure 1 we have maintained the frequency at 0 Hz. A similar plot (for another sandstone) is given in Santos et al. (1990b).

Next, we vary the frequency and show the dispersion characteristics of the P1 mode (Figure 2a). We present results in Figure 2a as percentage change over v_{p1} at the reference frequency of 1 Hz. In line with the other studies (Carcione et al., 2004), Figure 2a shows a step change in v_{p1} at 10 KHz. It is notable that the change is more significant for lower S_{nw} . The significance is that well-to-seismic tie can become more erroneous in formations with low gas saturation if capillary effects are not appropriately accounted for. The dispersion characteristics of the P2 and P3 modes (Figure 2b and 2c respectively) are such that v_{p2} and v_{p3} decrease as capillary pressure increases up to the characteristic frequency beyond which it becomes fairly constant. Further, the shear mode does not have any dispersive properties and thus it is not shown here.

We show the attenuation characteristics of the P1, P2 and P3 modes in Figures 3a, 3b and 3c. The attenuation of the P1 mode (Figure 3a) is more prominent at frequencies > 3 kHz and, least among all the three modes, increases as capillary pressure increases. This explains that the amplitude of the P1 mode is less affected by fluid viscosity and permeability (absolute and relative). The attenuation characteristics of the P2 mode vary across the entire frequency range and, similar to P1 mode, the attenuation factor of the P2 mode (most among all the three modes) increases as capillary pressure increases. This clearly shows that the amplitude of the P2 mode is dependent on saturation of the wetting phase (S_w). However, the attenuation of the P3 mode decreases as capillary pressure increases which in turn establishes that the amplitude of the P3 mode is dependent on the saturation of the non-wetting phase S_{nw} . The shear wave is not affected by the fluid phases and thus there is no effect of the varying capillary pressure on its phase velocity and attenuation.

Ravazzoli and Santos (2005) presented the theory of wave propagation in a rock saturated with two-phase fluids under variable pressure conditions, especially on \bar{p}_w . In this study, they found that the velocity and attenuation of P- (P1, P2 and P3) and shear waves also vary with \bar{p}_w . Accordingly, we also computed the simultaneous effect of capillary pressure (p_{ca}) and absolute pressure of the wetting fluid (\bar{p}_w) on the velocity of the P-wave modes (see Figure 4). Figure 4a shows the phase velocity of the P1 mode (computed at 1 MHz) against the capillary pressure p_{ca} at varying \bar{p}_w . The phase velocity of this mode decreases as \bar{p}_w increases, which is due to the fact that as \bar{p}_w increases p_{ca} decreases. This further corroborates the dispersion analysis of the P1 mode shown in Figure 2a. Figure 4b and 4c are plots of the phase velocities of the P2 and P3 modes, computed at variable p_{ca} and \bar{p}_w . As \bar{p}_w increases, the first velocity increases at low value of p_{ca} (low gas saturation), whereas at higher values of p_{ca} this velocity decreases. This reconfirms the results of the dispersion analysis for the P2 mode, shown in Figure 2b. The phase velocity of the P3 mode against \bar{p}_w is shown in Figure 4c. In general, there is a positive correlation with \bar{p}_w . This observation is in line with the dispersion analysis of the P3 mode (Figure 2c), showing a negative correlation with respect to p_{ca} .

Next, we perform numerical simulations but before we test the accuracy of the method. Analytical solutions of Equation (15) for the plane waves ((35) and (36)) are computed by solving a linear system of equations obtained after substituting Equations (35) and (36) into Equation (15). A plot showing the error between the numerical and analytical solutions of the solid particle velocity (v_x^s) versus the number of terms used in Fourier expansion (N_g), computed for values of CFL = 0.8 and 0.6, is shown in Figure 4. It is worth to note that as N_g increases the rate of convergence decreases to 4th-order but as time steps is increased (CFL=0.6) the convergence is improved. This proves our claim that the numerical scheme (Equation (34)) is of very high order and bounded by convergence not by stability. In addition to this, Figure 5 also proves that as the degree of freedom increases in space, the numerical scheme is gradually dominated by the order of the time accuracy.

We show the numerical simulation based on Equation (15) using a 400×400 grid domain at ultrasonic (300 kHz) and seismic (25 Hz) frequencies. The system of Equations (15) is solved numerically for a capillary pressure of 3.22 kPa ($S_{nw} = 10\%$) and 24.45 kPa ($S_{nw} = 50\%$). Snapshots of the particle velocity of the rock frame in the ultrasonic frequency range captured at $p_{ca} = 3.22$ kPa and 24.45 kPa, are shown in Figure 6a and 6b, respectively. Four wave modes P1, P2, P3 and S are marked on all the illustrations shown in Figures 6, 7 and 8. The P2 mode, generated due to the relative motion between the solid and the non-wetting phase, is the classical Biot *slow* P mode with polarity opposite to that of the fast compressional mode P1. The polarity of the P3 mode, generated due to relative motion between the solid and the wetting phase, shows a sync in polarity with the main compressional wave P1.

The attenuation characteristics shown in Figure 3 indicate that in the high-frequency range the amplitude of the P1 mode decreases as capillary pressure increases, which is validated from Figures 6a and 6b. Computed maximum absolute particle velocities of the P1 mode at $p_{ca} = 3.22$ kPa and $p_{ca} = 24.45$ kPa are 2×10^{-10} and 8×10^{-11} respectively. This proves the attenuation characteristic of the P1 mode with capillary pressure, obtained from the dispersion analysis.

In the high-frequency range the phase velocity of the P2 and P3 modes (Figure 2b and 2c) decreases as capillary pressure increases, which can be verified from numerical simulation as well. Apparently the distance traversed by P2 and P3 modes in Figure 5a is more than in Figure 6b, thus proving slow phase velocity for P2 and P3 modes as capillary pressure increases. In the high-frequency range, the attenuation of the P2 mode (Figure 3b) increases as capillary pressure increases, which can be validated from numerical simulation by extracting the maximum absolute particle velocity in Figure 6a and 6b. The absolute particle velocity of the P2 mode at $p_{ca} = 3.22$ kPa (Figure 6a) and 24.45 kPa (Figure 6b) is 7×10^{-10} and 3×10^{-10} respectively, which corroborates the observation from Figure 3b.

In the high-frequency range the attenuation of the P3 mode (Figure 3c) decreases as capillary pressure increases, opposite to the trend observed for the P2 mode. This phenomena correlates very well with the theory, stating that as saturation of non-wetting phase increases (capillary pressure increases) the existence of the P3 mode becomes more prominent due to the fact that P3 mode is the upshot of the relative motion among the particles of the non-wetting phases and the rock frame. The same concept is also applicable for the P2 mode. To corroborate the attenuation characteristics of the P3 mode with numerical simulations, we extracted the absolute particle velocities of the P3 mode from Figures 6a and Figure 6b. The absolute particle velocities of the P3 mode for $p_{ca} = 3.22$ kPa and 24.45 are 2×10^{-10} and 3×10^{-10} respectively, which justifies the dispersion results for the P3 mode.

Figures 6c and 6d shows snapshot (at 1 s) of the horizontal component of the particle velocity (v_x^s) of the rock frame at 25Hz simulated for $p_{ca} = 3.22$ kPa and 24.45 kPa respectively. The phase velocity of the P1 mode (Figure 2a) at 25 Hz varies from 1780 m/s to 1805 m/s with p_{ca} varying from 3.22 kPa to 24.45 kPa. A subtle difference of 25 m/s of velocity between $p_{ca} = 3.22$ kPa and 24.45 kPa is reflected as 1.5 spatial grids in the domain of numerical simulation, which is very hard to visualize in image but a careful examination of Figure 6d shows that the P1 mode traversed more distance than the P1 mode in Figure 6c. The phase velocity of the P2 (Figure 2b) and P3 (Figure 2c) modes at 25 Hz is ≈ 0 , thus the medium does not support the propagation of slow P modes in the low-frequency range. The attenuation factor of the P2 mode is 40 at $p_{ca} = 3.22$ kPa and 24.45 kPa, which is more than the attenuation factor (≈ 0) of the P1 mode. This is the effect of capillary pressure on the existence of the P2 mode, which does not appear in the numerical simulation shown in Figures 6c and 6d. The attenuation characteristic of the P3 mode with varying capillary pressure shows the same pattern as the P2 mode and also does not appear in the numerical simulation shown in Figure 6(c) and 6(d).

Figure 7 shows snapshots of the horizontal particle velocity (v_x^n) for the non-wetting phase. Figures 7a and 7b show that, at high frequencies, the P2 and P3 modes are much stronger in the fluid phases. As capillary pressure increases, the energy contained in the P2 and P3 modes increase, which can be verified by an analysis of the relative amplitudes between the slow (P2 and P3) modes and the fast (P1) mode. The relative amplitude between Figures 6a and 7a is 1179, whereas the relative amplitude between Figures 6b and 7b is 1200. This justifies our observation of the effect of capillary pressure on the energy contained in the P2 and P3 modes present in the fluid phases. In the low-frequency range (Figures 7c and 7d), the P2 and P3 modes do not propagate, remaining static and diffusing gradually. The maximum energy is concentrated in the solid phase and is invariable with the capillary pressure.

Figure 8 shows snapshots of the horizontal particle velocity (v_x^w) for the wetting phase. Like in the non-wetting phase at high frequencies, the energy is concentrated mainly in the P2 and P3 modes (Figure 7a and Figure 7b). The relative amplitude between Figures 6a and 8a is 64, which decreases to 52 between Figures 6b and 8b. Thus, as capillary pressure increases, the energy contained in the P2 and P3 modes decreases. In the low-frequency range (Figure 8c and 8d), the physics of the P2 and P3 mode remains same as in the non-wetting phase. Though the gradual increase of the non-wetting saturation S_{nw} increases the concentration of energy in the non-wetting phases, it will never be zero due to the presence of irreducible saturation. Thus, the numerical simulation will not reduce to the classical Biot's case.

Shot gathers representing the horizontal particle motion of the rock frame are shown in Figure 9 and 10 for

the high and low-frequency cases, respectively. These shot gathers, in general, show a stronger shear mode as they represent the horizontal component of the rock frame velocity (v_x^s). The polarity of the wave modes on either side of the origin (offset = 0 m) is phased out by 180° due to the fact that the polarization vector on either side of the origin is in the opposite direction. The shot gathers shown in Figures 9 and 10 are simulated for homogeneous medium and modes recorded P1, P2, P3 and S modes are direct arrivals from the source. As expected from previous results (Figures 6-8) the P1, P2 and P3 modes are well identified in the high-frequency case (Figure 9), whereas the P and S modes are more dominant in the low-frequency case. In Figure 9 and 10, the variation of amplitude agrees with the results shown in Figure 2 and 3.

6. DISCUSSION

The effects of multiphase fluids in a porous rock, e.g., wettability, capillary pressure and inter-facial tension has been shown in various physical process, e.g. transport of electric current through porous media (Cai et al., 2017), capillary imbibition in porous media (Cai and Yu, 2011) and spontaneous co-current imbibition (Cai et al., 2010). In this study, we have shown the dependence of the phase velocities on capillary pressure for reservoir rocks saturated with multi-phase fluids. Capillary pressure arises due to the pressure difference across the contact interface between the wetting and non-wetting phases and thus it is a monotonically increasing function of the saturation of the non-wetting phase Santos et al. (2004). Figure 1 shows plots of the rock frame velocity v_{p1} , known as P-wave velocity in various acoustic and elastic seismic modeling, versus increasing saturation of the non-wetting phase (S_{nw}), which is directly proportional to capillary pressure. Figure 1 is in concordance with the fluid substitution model of Gassmann's (Gassmann, 1951). The velocity (v_{p1}) in the present study is obtained from the model developed by Santos et al. (1990b) which assumes a poromechanical approach for deriving the constitutive equations. An effect of the pore topology on v_{p1} with increasing gas saturation or capillary pressure is not yet explained.

To incorporate the effect of pore topology, we computed the velocity of the reservoir sandstone (Table 1) using the Hashin-Strickman (HS) model (Hashin and Shtrikman, 1963). A plot comparing the wet-rock velocity v_{p1} obtained from Equation (18) and the velocity obtained from the HS model is shown in Figure 11. The velocity obtained from this model over predicts the velocity as it does not incorporate the effect of capillary pressure on the particle motion. Thus the velocity model with respect to capillary pressure shown in Figure 1 is more accurate over any static or quasi-static model such than that of the HS model.

The model used in the present study is based on the assumption that pores are completely connected and any isolated pores are part of the matrix mineral. Thus, the velocity model presented in Figure 1 may not be able to correctly predict the velocity in low permeability reservoir rocks such as shale, tight carbonates and sands, unless the mineral properties are accurately obtained. In addition to that, the model also assumes that the saturation of the non-wetting phase (S_{nw}) does not account for the effect of interstitial micro gas bubbles present in the wetting phase. As Kepkay and Cooke (1978) proved, the velocity of sound notably depends on the concentration of micro gas bubbles present in the wetting phase along with the total gas volume. Thus, the results of velocity model obtained in this study may not be able to explain the effect of micro gas bubble, unless a suitable model to obtain the wetting phase properties is used.

The applicability of the velocity model presented here spans from hydrocarbon exploration to near-surface exploration. Well to seismic tie, an important part of seismic interpretation, is carried out by correlating the sonic log with surface seismic. The mapping of velocity between the sonic range, recorded from sources at ultrasonic frequencies, and surface seismic (obtained from low-frequency sources) does not account for the effect of capillary pressure on velocity obtained from the sonic log. The correct practice to tie the well and seismic data will require an upscaling of the velocity with a-priori information of the saturations in the reservoir zone. The other application comes from near-surface exploration wherein we are interested in the top few meters (0 -10 m) of the subsurface. Seismic data recorded in the near surface setting presumably contains frequencies more than deep seismic data. Thus, wave propagation in the near surface medium may fall in the high-frequency regime. A capillary pressure dependent velocity model may be applicable under two conditions. First, in the presence of a fine grained soil as soil is saturated above the water table due to capillary rise and is under negative pore pressure. Second, in the presence of a coarse grain soil wherein the water will drain from the pores above the water table and thus air will fill the pores of the soil above the

water table. These two conditions could be approximated by the presented model. In this work we consider the effect of capillary pressure at a macroscopic scale. Another, indirect but possibly stronger effect is the influence of capillary pressure on fluid flow (Macias et al., 2015). In this case partial saturation is affected by the capillary forces inducing mesoscale heterogeneities and fluid patches. Seismic velocity is affected by partial saturation and anelasticity.

In another line of application, the velocity and attenuation model presented here can be used to study the spontaneous imbibition, responsible for the main mechanism of oil production from fractures. Meng et al. (2017) has shown that capillary pressure is one of the primary factors responsible for spontaneous imbibition, which, as shown in the present study, varies with the saturation of the wetting and non-wetting fluids. Thus, in events of enhanced oil recovery processes (4D time-lapse seismic study) the aided volume of hydrocarbon due to spontaneous imbibition, can be estimated by considering the effect of capillary pressure in seismic velocity (Figure 2 and 3).

7. CONCLUSIONS

We have analyzed the dependence of the phase velocity and attenuation in rocks saturated with multi-phase fluids. We also presented numerical simulations of wave propagation at varying capillary pressures. We observed that in the high-frequency range, as capillary pressure increases, the phase velocity of the P1 mode increases and the velocities of the slow P modes (P2 and P3) decrease substantially. In the high-frequency range, the attenuation of the P1 and P3 modes decreases with capillary pressure, whereas the attenuation of the P2 modes increases. In the low-frequency range, the velocity of the P1 mode increases but remain constant up to the characteristic frequency. The velocity of the P2 mode decreases with increasing capillary pressure but increases gradually with frequency, whereas the velocity of the P3 mode has opposite characteristic than that of the P2 mode. The attenuation of the P1, P2 and P3 modes have no much notable effect. We also validate the dispersion and attenuation relation with numerical solutions of the wave equations at varying capillary pressures. Moreover, we analyzed the velocity of the P1 mode of the wet-rock with respect to the gas saturation and compared this with topology-based models such as the Hashin-Shtrickman one. The velocity obtained from the HS model over predicts the actual velocity due to the non-inclusion of the capillary pressure.

8. ACKNOWLEDGEMENT

This is Boone Pickens School of Geology, Oklahoma State University, contribution number 2018-85.

REFERENCES

- Allard, J. and Atalla, N., *Propagation of sound in porous media: modelling sound absorbing materials*, John Wiley & Sons, 2009.
- Auriault, J.L., Lebaigue, O., and Bonnet, G., Dynamics of two immiscible fluids flowing through deformable porous media, *Transport in Porous Media*, vol. **4**, no. 2, pp. 105–128, 1989.
- Berryman, J.G., Confirmation of biot's theory, *Applied Physics Letters*, vol. **37**, no. 4, pp. 382–384, 1980.
- Biot, M.A., Theory of propagation of elastic waves in a fluid-saturated porous solid. i. low-frequency range, *The Journal of the Acoustical Society of America*, vol. **28**, no. 2, pp. 168–178, 1956a.
- Biot, M.A., Theory of propagation of elastic waves in a fluid-saturated porous solid. ii. higher frequency range, *The Journal of the Acoustical Society of America*, vol. **28**, no. 2, pp. 179–191, 1956b.
- Biot, M.A., Mechanics of deformation and acoustic propagation in porous media, *Journal of Applied Physics*, vol. **33**, no. 4, pp. 1482–1498, 1962.
- Cai, J., Wei, W., Hu, X., and Wood, D.A., Electrical conductivity models in saturated porous media: a review, *Earth-Science Reviews*, vol. **171**, pp. 419–433, 2017.
- Cai, J. and Yu, B., A discussion of the effect of tortuosity on the capillary imbibition in porous media, *Transport in Porous Media*, vol. **89**, pp. 251–263, 2011.
- Cai, J., Yu, B., Zou, M., and Luo, L., Fractal characterization of spontaneous co-current imbibition in porous media, *Energy & Fuels*, vol. **24**, no. 3, pp. 1860–1867, 2010.
- Carcione, J., *Wave Fields in Real Media: Wave Propagation in Anisotropic, Anelastic, Porous and Electromagnetic Media*, Elsevier Science, 2014.
- Carcione, J.M., Cavallini, F., Santos, J.E., Ravazzoli, C.L., and Gauzellino, P.M., Wave propagation in partially saturated porous media: simulation of a second slow wave, *Wave Motion*, vol. **39**, no. 3, pp. 227–240, 2004.
- Carcione, J.M., Herman, G.C., and Ten Kroode, A., Seismic modeling, *Geophysics*, vol. **67**, no. 4, pp. 1304–1325, 2002.
- Carcione, J.M. and Quiroga-Goode, G., Some aspects of the physics and numerical modeling of biot compressional waves, *Journal of Computational Acoustics*, vol. **3**, no. 04, pp. 261–280, 1995.
- Carcione, J.M. and Seriani, G., Wave simulation in frozen porous media, *Journal of Computational Physics*, vol. **170**, no. 2, pp. 676–695, 2001.
- Dejam, M., Hassanzadeh, H., and Chen, Z., Capillary forces between two parallel plates connected by a liquid bridge, *Journal of Porous Media*, vol. **18**, no. 3, pp. 179–188, 2015.
- Domenico, S., Effect of brine-gas mixture on velocity in an unconsolidated sand reservoir, *Geophysics*, vol. **41**, no. 5, pp. 882–894, 1976.
- Domenico, S., Elastic properties of unconsolidated porous sand reservoirs, *Geophysics*, vol. **42**, no. 7, pp. 1339–1368, 1977.
- Gassmann, F., Über die elastizität poroser medien, *Vierteljahrsschrift der Naturforschenden Gesellschaft in Zürich*, vol. **96**, pp. 1–23, 1951.
- Gomez, C.T., Dvorkin, J., and Vanorio, T., Laboratory measurements of porosity, permeability, resistivity, and velocity on fontainebleau sandstones, *Geophysics*, vol. **75**, pp. E191–E204, 2010.
- Hashin, Z. and Shtrikman, S., A variational approach to the theory of the elastic behaviour of multiphase materials, *Journal of the Mechanics and Physics of Solids*, vol. **11**, no. 2, pp. 127–140, 1963.
- Jain, M.K., *Numerical solution of differential equations*, Wiley Eastern Ltd., 1979.
- Johnson, D.L., Koplik, J., and Dashen, R., Theory of dynamic permeability and tortuosity in fluid-saturated porous media, *Journal of Fluid Mechanics*, vol. **176**, pp. 379–402, 1987.
- Kelder, O. and Smeulders, D.M., Observation of the biot slow wave in water-saturated nivelsteiner sandstone, *Geophysics*, vol. **62**, no. 6, pp. 1794–1796, 1997.
- Kepkay, P. and Cooke, R., Velocity of sound as a function of bubble distribution in gas-bearing sediments, *Geophysical Research Letters*, vol. **5**, no. 12, pp. 1071–1073, 1978.
- Liu, J., Müller, T.M., Qi, Q., Lebedev, M., and Sun, W., Velocity-saturation relation in partially saturated rocks: Modelling the effect of injection rate changes, *Geophysical Prospecting*, vol. **64**, no. 4, pp. 1054–1066, 2016.

- Lo, W.C., Sposito, G., and Majer, E., Wave propagation through elastic porous media containing two immiscible fluids, *Water Resources Research*, vol. **41**, W02025, no. 2, 2005.
- Lu, J.F., Hanyga, A., and Jeng, D.S., A mixture-theory-based dynamic model for a porous medium saturated by two immiscible fluids, *Journal of Applied Geophysics*, vol. **62**, no. 2, pp. 89–106, 2007.
- Macias, L.A., Savioli, G.B., Santos, J.E., Carcione, J.M., and Gei, D., Analysis of capillary pressure effect on the seismic response of a co 2-storage site applying multiphase flow and wave propagation simulators, *International Journal of Greenhouse Gas Control*, vol. **39**, pp. 335–348, 2015.
- Meng, Q., Liu, H., and Wang, J., A critical review on fundamental mechanisms of spontaneous imbibition and the impact of boundary condition, fluid viscosity and wettability, *Advances in Geo-energy Research*, vol. **1**, pp. 1–17, 2017.
- Mochizuki, S., Attenuation in partially saturated rocks, *Journal of Geophysical Research: Solid Earth*, vol. **87**, no. B10, pp. 8598–8604, 1982.
- Oura, H., Sound velocity in the snow cover, *Low Temperature Science. Series A, Physical Sciences*, vol. **9**, pp. 171–178, 1952.
- Papageorgiou, G. and Chapman, M., Wave-propagation in rocks saturated by two immiscible fluids, *Geophysical Journal International*, vol. **209**, no. 3, pp. 1761–1767, 2017.
- Plona, T.J., Observation of a second bulk compressional wave in a porous medium at ultrasonic frequencies, *Applied Physics Letters*, vol. **36**, no. 4, pp. 259–261, 1980.
- Qi, Q., Müller, T.M., Gurevich, B., Lopes, S., Lebedev, M., and Caspari, E., Quantifying the effect of capillarity on attenuation and dispersion in patchy-saturated rocks, *Geophysics*, vol. **79**, no. 5, pp. WB35–WB50, 2014.
- Ravazzoli, C. and Santos, J., A theory for wave propagation in porous rocks saturated by two-phase fluids under variable pressure conditions, *Bolletino di Geofisica Teorica ed Applicata*, vol. **46**, pp. 261–285, 2005.
- Ravazzoli, C., Santos, J., and Carcione, J., Acoustic and mechanical response of reservoir rocks under variable saturation and effective pressure, *The Journal of the Acoustical Society of America*, vol. **113**, no. 4, pp. 1801–1811, 2003.
- Santos, J.E., Corberó, J.M., and Douglas Jr, J., Static and dynamic behavior of a porous solid saturated by a two-phase fluid, *The Journal of the Acoustical Society of America*, vol. **87**, no. 4, pp. 1428–1438, 1990a.
- Santos, J.E., Douglas Jr, J., Corberó, J., and Lovera, O.M., A model for wave propagation in a porous medium saturated by a two-phase fluid, *The Journal of the Acoustical Society of America*, vol. **87**, no. 4, pp. 1439–1448, 1990b.
- Santos, J.E., Gauzellino, P.M., Savioli, G.B., and Martínez Corredor, R., Numerical simulation in applied geophysics, *Journal of Computer Science & Technology*, vol. **13**, pp. 137–142, 2013.
- Santos, J.E., Gauzellino, P.M., Savioli, G.B., and Martínez Corredor, R., *Numerical Simulation in Applied Geophysics*, Springer, 2016.
- Santos, J.E., Ravazzoli, C.L., Gauzellino, P.M., Carcione, J.M., and Cavallini, F., Simulation of waves in poro-viscoelastic rocks saturated by immiscible fluids: numerical evidence of a second slow wave, *Journal of Computational Acoustics*, vol. **12**, no. 01, pp. 1–21, 2004.
- Santos, J.E., Savioli, G.B., and Martínez Corredor, R., 2017. Slow waves in a poroelastic solid saturated by multiphase fluids. *Poromechanics VI*. pp. 1674–1681.
- Stoll, R.D. and Bryan, G.M., Wave attenuation in saturated sediments, *The Journal of the Acoustical Society of America*, vol. **47**, no. 5B, pp. 1440–1447, 1970.
- Tian, Y.C., Ma, J.W., and Yang, H.Z., Wavefield simulation in porous media saturated with two immiscible fluids, *Applied Geophysics*, vol. **7**, no. 1, pp. 57–65, 2010.

LIST OF TABLES

1. Material properties of the Nivelsteiner sandstone

Article in Press

LIST OF FIGURES

1. Phase velocity of the P1 mode computed at 0 Hz as a function of the saturation of the non-wetting phase.
2. Effect of the capillary pressure on (a) the velocity of the fast P1- mode, (b) the velocity of the slow P2-mode and (c) the velocity of the slow P3 mode. Note that different capillary pressures correspond to different saturations of the non-wetting (gas) phase (S_{nw}).
3. Effect of the capillary pressure on (a) the attenuation of the fast P1- mode, (b) the attenuation of the slow P2-mode and (c) the attenuation of the slow P3 mode. Note that different capillary pressures correspond to different saturations of the non-wetting (gas) phase (S_{nw}).
4. Simultaneous effect of capillary pressure and absolute wetting fluid pressure (p_w) on (a) the velocity of the fast P1- mode, (b) the velocity of the slow P2-mode and (c) the velocity of the slow P3 mode. Velocity is computed at frequency of 1 MHz. Note that different absolute wetting fluid pressure (p_w) correspond to different depths of the reservoir rocks.
5. Convergence plot between the norm of error of solid velocity and number of term used in Fourier expansion (N_g). Convergence is computed for CFL = 0.8 and CFL = 0.6. (CFL: Courant-Friedrich-Lewy number).
6. Horizontal component of the particle velocity v_x . (a) and (b) are snapshots at 18 μ s for a 300 kHz Ricker source wavelet. (c) and (d) are snapshots at 1 s for a 25 Hz Ricker source wavelet. In (a) and (b) the mesh size is 0.18 mm and the size of the time step is 12.5 ns. In (c) and (d) the mesh size is 15 m and the size of the time step (dt) is 1 ms. In (a) and (c) $S_{nw} = 10\%$ and in (b) and (d) $S_{nw} = 50\%$.
7. Horizontal component of the particle velocity v_x^n . (a) and (b) are snapshots at 18 μ s for a 300 kHz Ricker source wavelet. (c) and (d) are snapshots at 1 s for a 25 Hz Ricker source wavelet. In (a) and (b) the mesh size is 0.18 mm and the size of time step is 12.5 ns. In (c) and (d) the mesh size is 15 m and the size of time step (dt) is 1 ms. In (a) and (c) $S_{nw} = 10\%$ and in (b) and (d) $S_{nw} = 50\%$.
8. Horizontal component of the particle velocity v_x^w . (a) and (b) are snapshots at 18 μ s for a 300 KHz Ricker source wavelet. (c) and (d) are snapshots at 1 s for a 25 Hz Ricker source wavelet. In (a) and (b) the mesh size is 0.18 mm and the size of time step is 12.5 ns. In (c) and (d) the mesh size is 15 m and the size of time step (dt) is 1 ms. In (a) and (c) $S_{nw} = 10\%$ and in (b) and (d) $S_{nw} = 50\%$.
9. Shot gather of the particle velocity at ultrasonic frequencies, v_x^s . In (a) and (b) $S_{nw} = 10\%$ and in (b) and (d) $S_{nw} = 50\%$.
10. Shot gather of the particle velocity at seismic frequencies, v_x^s . In (a) and (b) $S_{nw} = 10\%$ and in (b) and (d) $S_{nw} = 50\%$.
11. Plot comparing the phase velocity of the P1 mode of the wet rock and that of the Hashin-Shtrickman (HS) model.

TABLE 1: Material properties of the Nivelsteiner sandstone

Medium properties		
Grain	Bulk Modulus, K_s (GPa)	36
	Density, ρ_s (kg/m^3)	2650
Matrix	Bulk Modulus, K_m (GPa)	6.21
	Shear Modulus, N (GPa)	4.55
	Porosity, ϕ	0.33
	Permeability κ (Darcy)	5
Gas (non-wetting phase)	Bulk Modulus, K_n (GPa)	0.022
	Density, ρ_n (kg/m^3)	100
	Viscosity, η_n (cP)	0.015
Water (wetting phase)	Bulk Modulus, K_w (GPa)	2.223
	Density, ρ_w (kg/m^3)	1000
	Viscosity, η_w (cP)	1

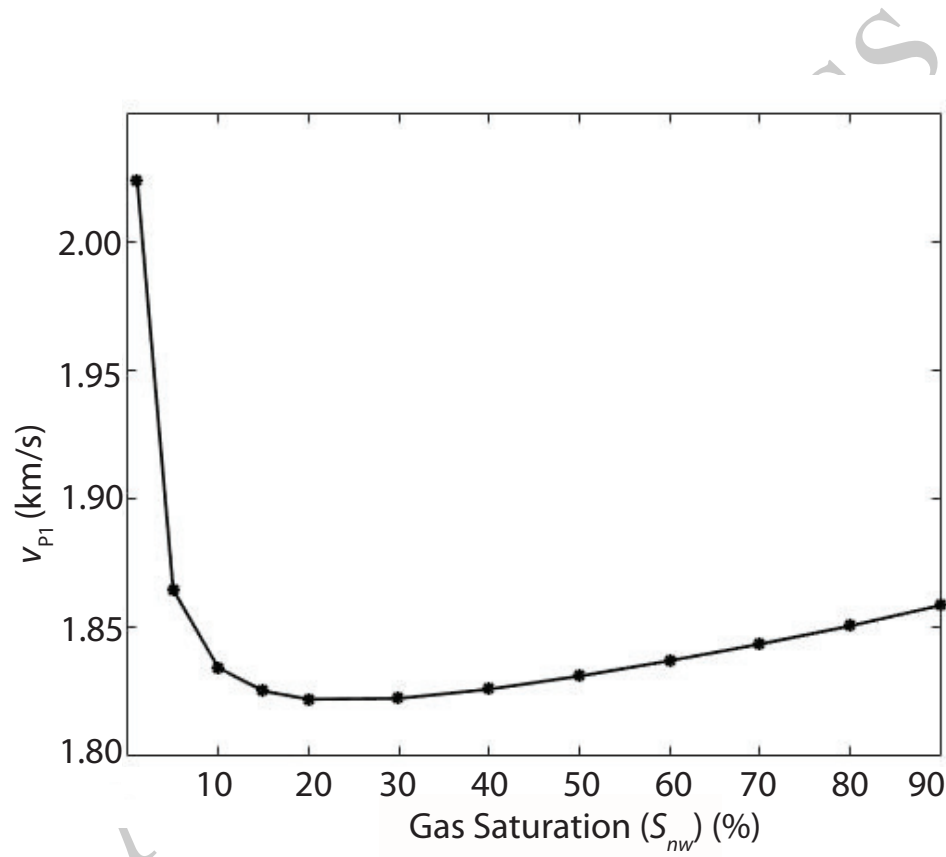


FIG. 1: Phase velocity of the P1 mode computed at 0 Hz as a function of the saturation of the non-wetting phase.

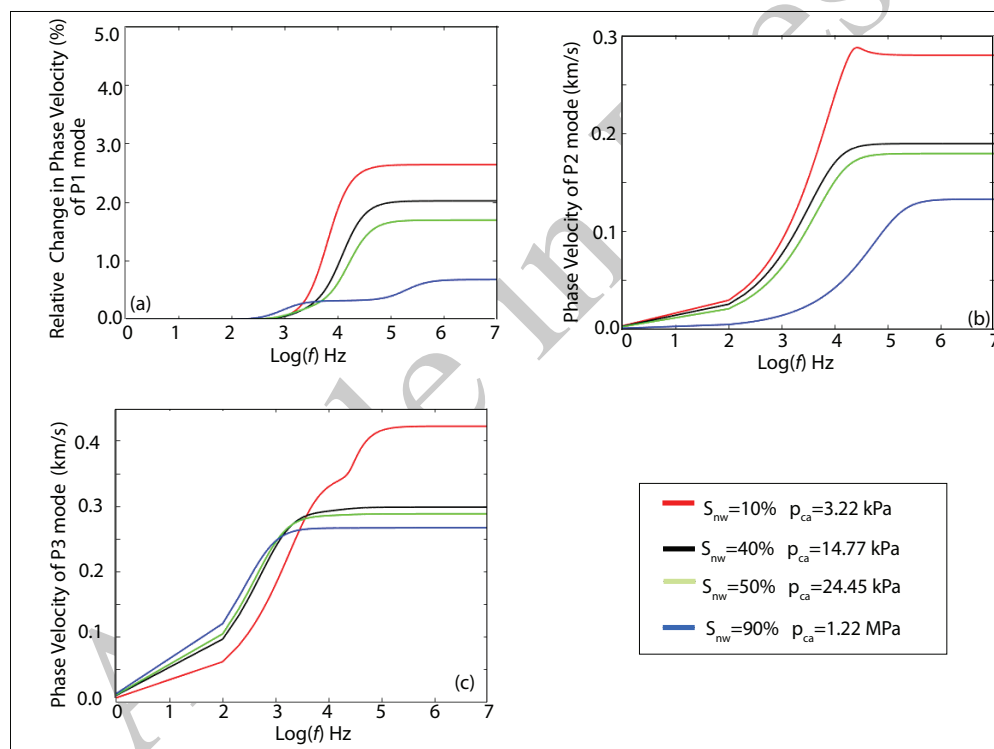


FIG. 2: Effect of the capillary pressure on (a) the velocity of the fast P1- mode, (b) the velocity of the slow P2-mode and (c) the velocity of the slow P3 mode. Note that different capillary pressures correspond to different saturations of the non-wetting (gas) phase (S_{nw}).

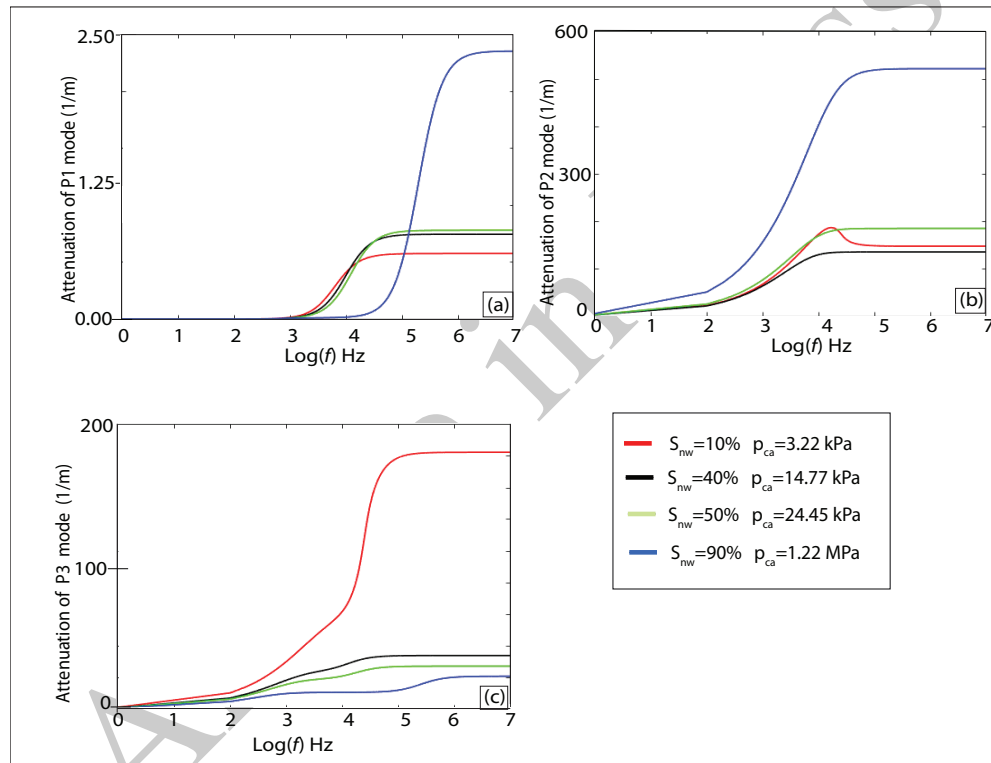


FIG. 3: Effect of the capillary pressure on (a) the attenuation of the fast P1- mode, (b) the attenuation of the slow P2-mode and (c) the attenuation of the slow P3 mode. Note that different capillary pressures correspond to different saturations of the non-wetting (gas) phase (S_{nw}).

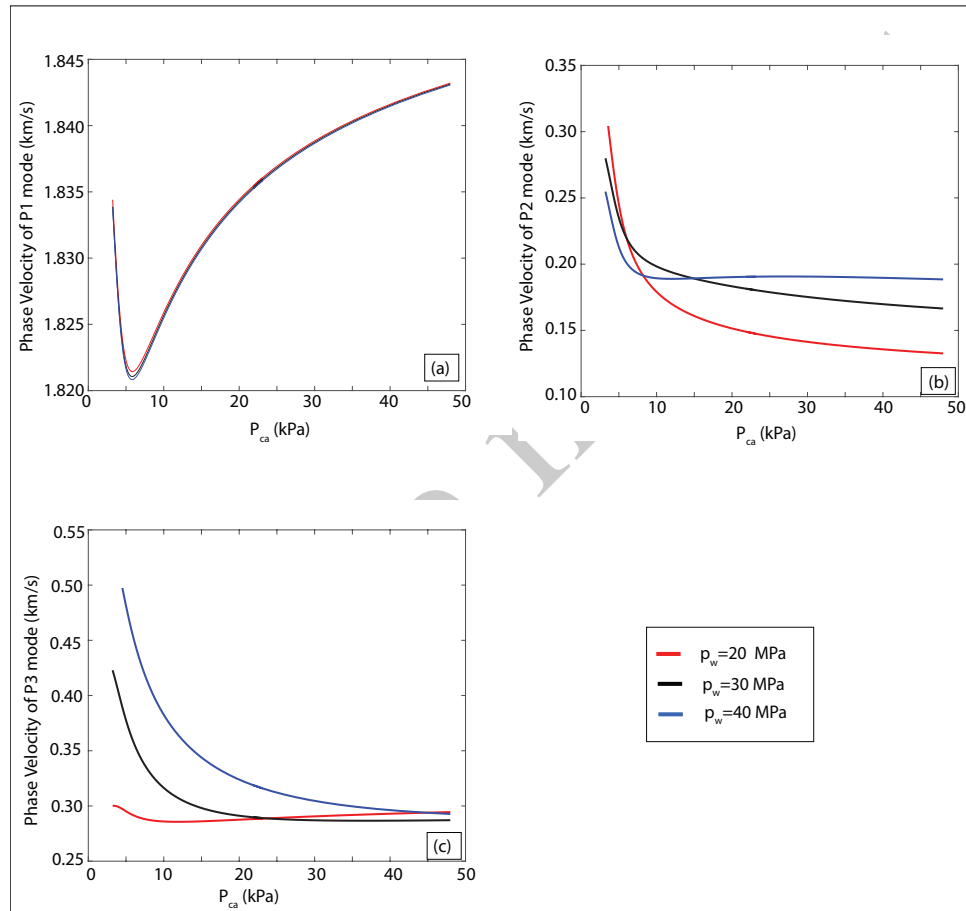


FIG. 4: Simultaneous effect of capillary pressure and absolute wetting fluid pressure (p_w) on (a) the velocity of the fast P1- mode, (b) the velocity of the slow P2-mode and (c) the velocity of the slow P3 mode. Velocity is computed at frequency of 1 MHz. Note that different absolute wetting fluid pressure (p_w) correspond to different depths of the reservoir rocks.

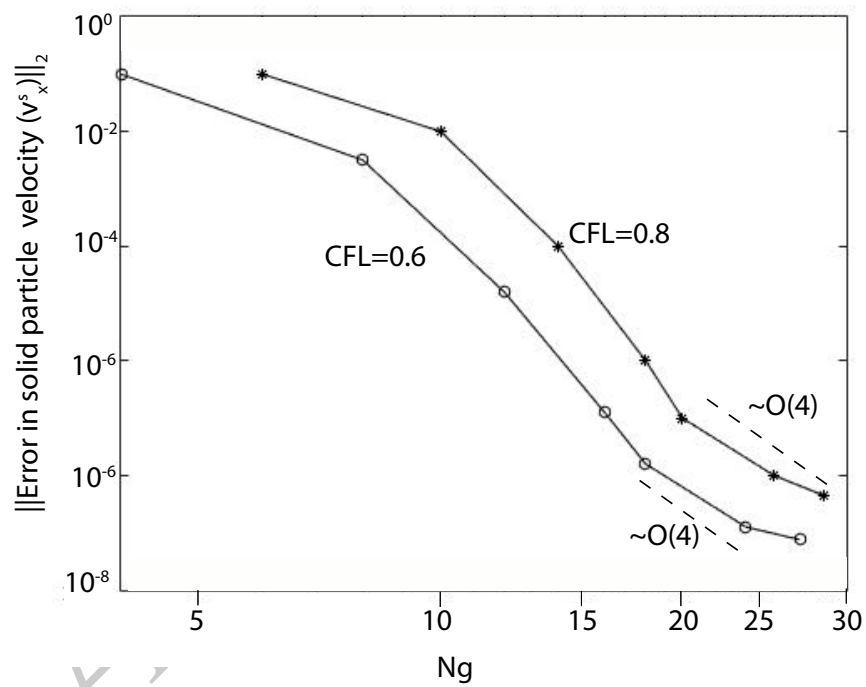


FIG. 5: Convergence plot between the norm of error of solid velocity and number of term used in Fourier expansion (N_g). Convergence is computed for CFL = 0.8 and CFL = 0.6. (CFL: Courant-Friedrich-Lewy number).

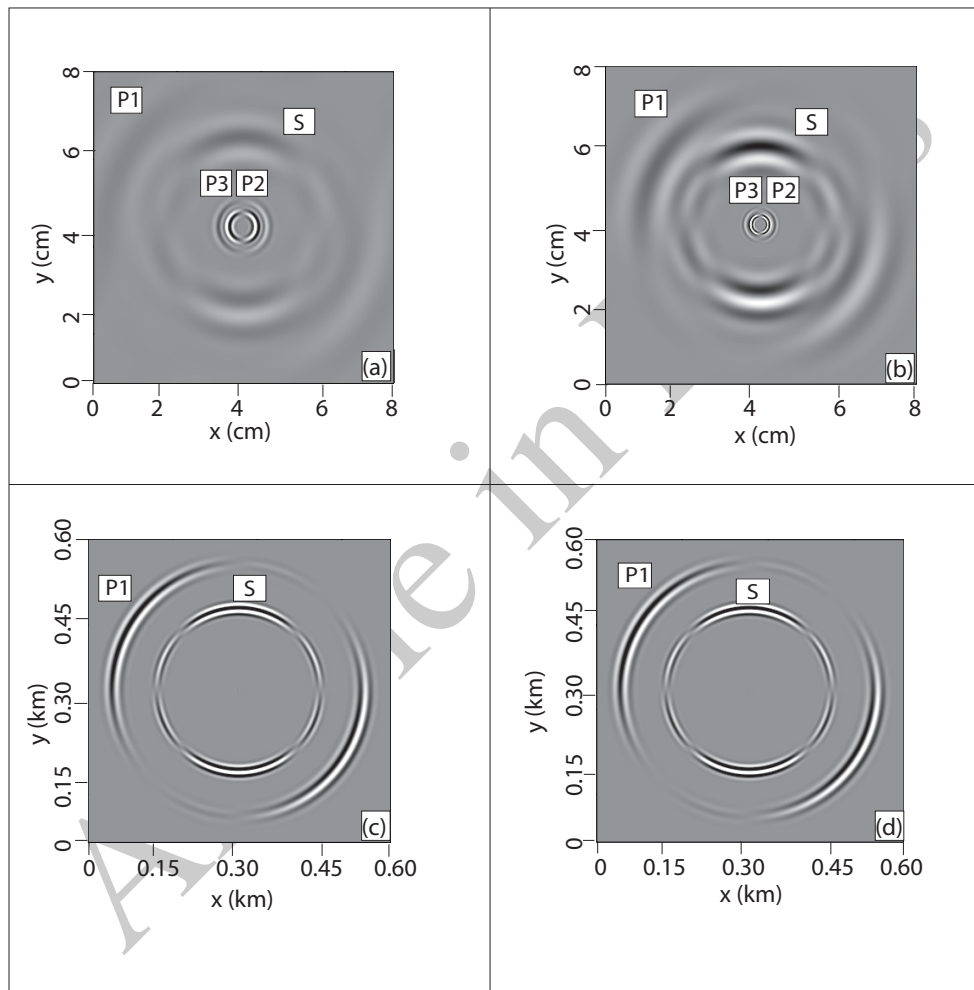


FIG. 6: Horizontal component of the particle velocity v_x . (a) and (b) are snapshots at $18 \mu\text{s}$ for a 300 kHz Ricker source wavelet. (c) and (d) are snapshots at 1 s for a 25 Hz Ricker source wavelet. In (a) and (b) the mesh size is 0.18 mm and the size of the time step is 12.5 ns. In (c) and (d) the mesh size is 15 m and the size of the time step (dt) is 1 ms. In (a) and (c) $S_{nw} = 10\%$ and in (b) and (d) $S_{nw} = 50\%$.

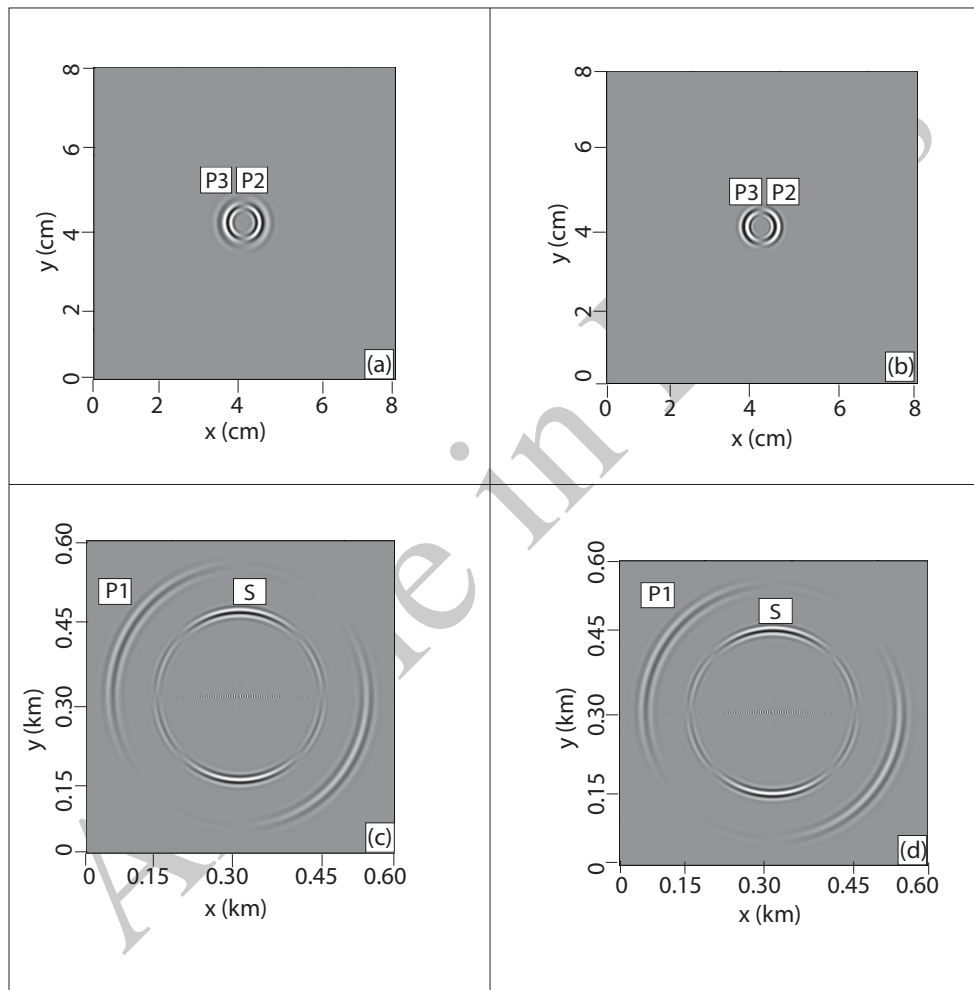


FIG. 7: Horizontal component of the particle velocity v_x^z . (a) and (b) are snapshots at $18 \mu\text{s}$ for a 300 kHz Ricker source wavelet. (c) and (d) are snapshots at 1 s for a 25 Hz Ricker source wavelet. In (a) and (b) the mesh size is 0.18 mm and the size of time step is 12.5 ns. In (c) and (d) the mesh size is 15 m and the size of time step (dt) is 1 ms. In (a) and (c) $S_{nw} = 10\%$ and in (b) and (d) $S_{nw} = 50\%$.

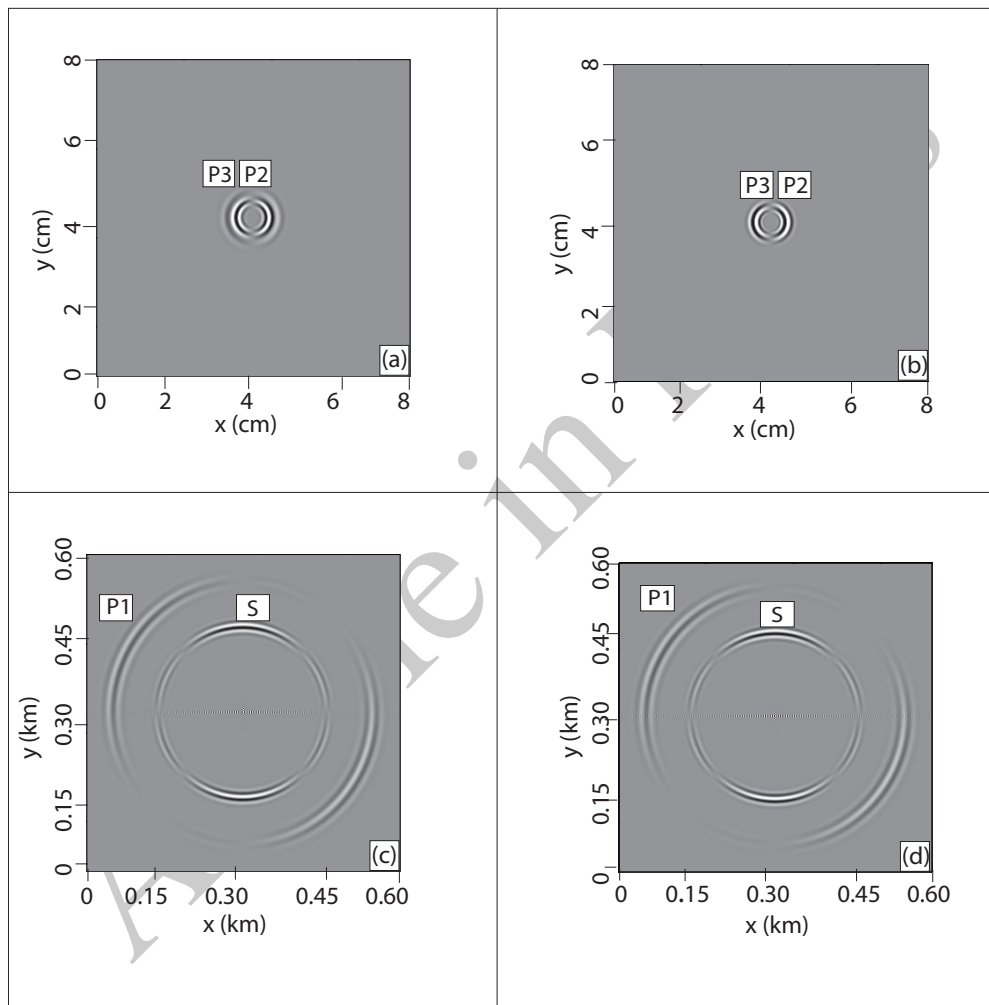


FIG. 8: Horizontal component of the particle velocity v_x^w . (a) and (b) are snapshots at $18 \mu\text{s}$ for a 300 kHz Ricker source wavelet. (c) and (d) are snapshots at 1 s for a 25 Hz Ricker source wavelet. In (a) and (b) the mesh size is 0.18 mm and the size of time step is 12.5 ns. In (c) and (d) the mesh size is 15 m and the size of time step (dt) is 1 ms. In (a) and (c) $S_{nw} = 10\%$ and in (b) and (d) $S_{nw} = 50\%$.

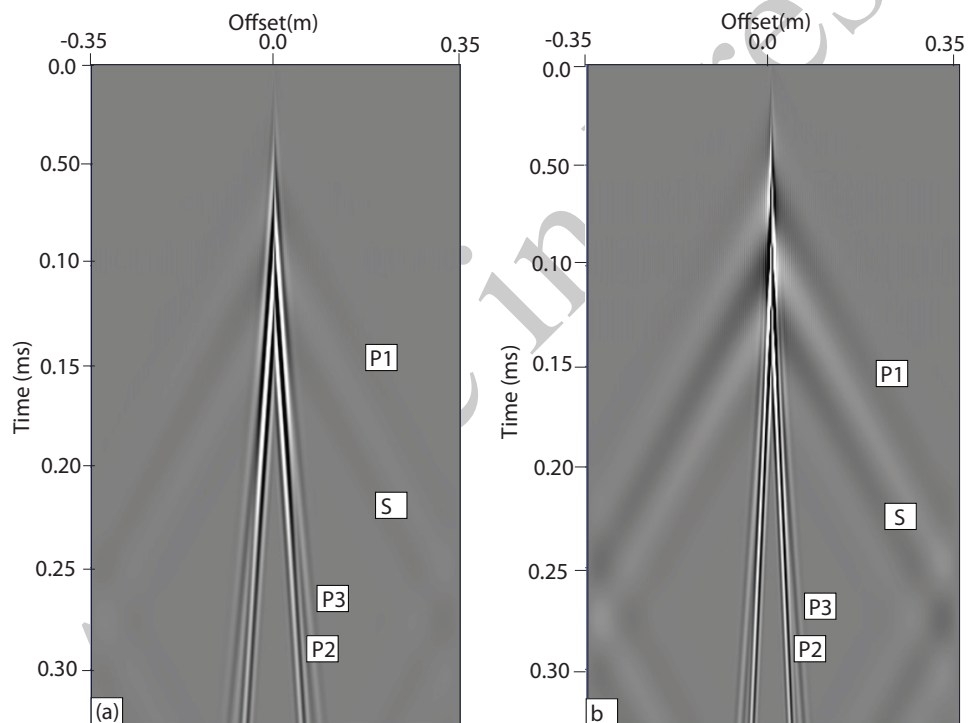


FIG. 9: Shot gather of the particle velocity at ultrasonic frequencies, v_x^s . In (a) and (b) $S_{nw} = 10\%$ and in (b) and (d) $S_{nw} = 50\%$.

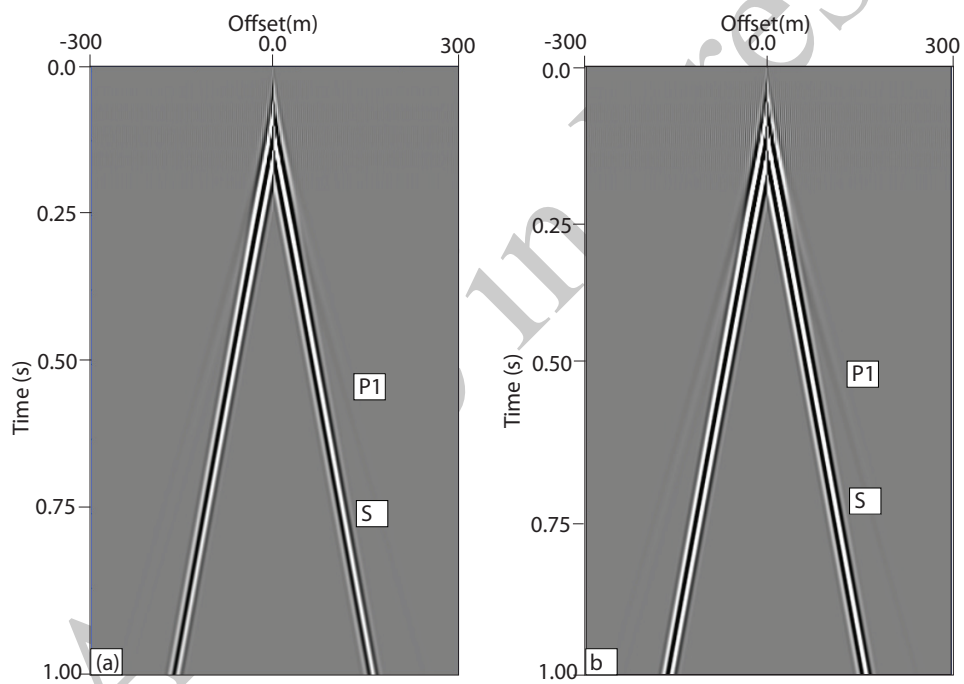


FIG. 10: Shot gather of the particle velocity at seismic frequencies, v_x^s . In (a) and (b) $S_{nw} = 10\%$ and in (b) and (d) $S_{nw} = 50\%$.

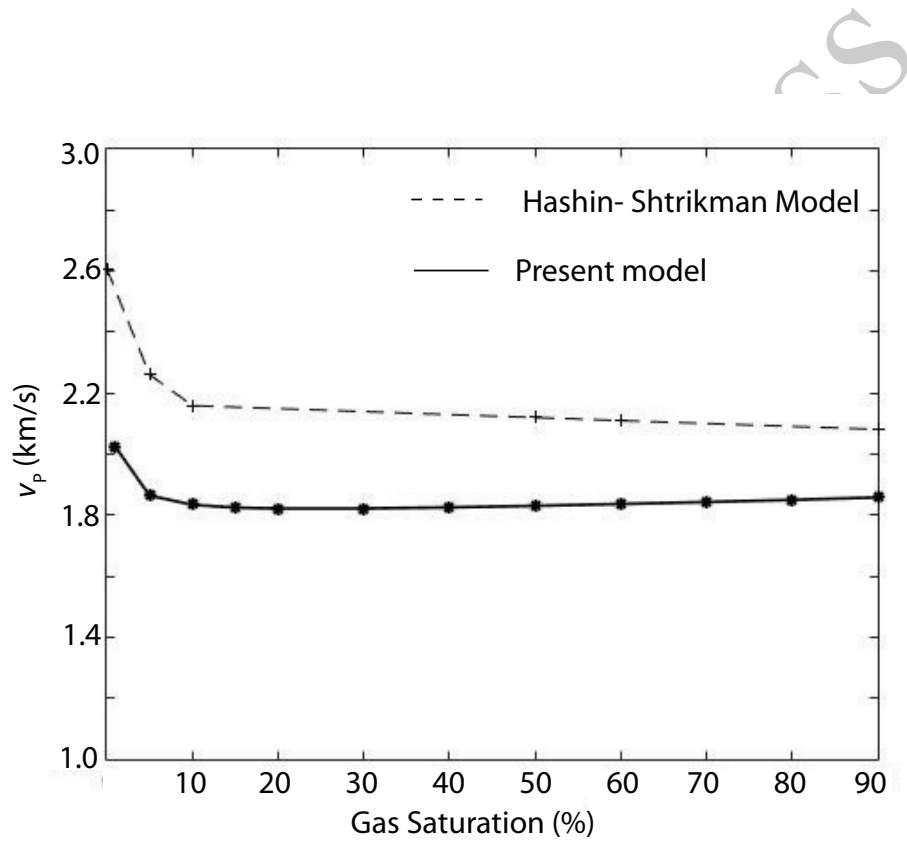


FIG. 11: Plot comparing the phase velocity of the P1 mode of the wet rock and that of the Hashin-Shtrickman (HS) model.